



# Numerical simulations of complex water spray flows around aircraft landing tire



Xiangshan Guan <sup>a</sup>, Weiwen Zhao <sup>b</sup>, Decheng Wan <sup>b,d,\*</sup>, Fei Xu <sup>c</sup>, Jie Liu <sup>e</sup>

<sup>a</sup> School of Ocean Engineering and Technology, Sun Yat-sen University, Zhuhai 519082, China

<sup>b</sup> Computational Marine Hydrodynamics Lab (CMHL), School of Naval Architecture, Ocean and Civil Engineering, Shanghai Jiao Tong University, Shanghai 200240, China

<sup>c</sup> School of Astronautics, Northwestern Polytechnical University, Xi'an 710072, China

<sup>d</sup> Ocean College, Zhejiang University, Zhoushan, 316021, China

<sup>e</sup> Commercial Aircraft Corporation of China, Ltd., Shanghai 200126, China

## ARTICLE INFO

### Article history:

Available online 13 September 2022

### Keywords:

Tire water spray  
SPH-FE coupling method  
Engine flow field  
Splashing trajectory  
Water inflow of engine

## ABSTRACT

When an aircraft passes through the contaminated runway, the water spray generated by the landing gear may enter the inlet of the engine and affect the operation of the engine. In this paper, the formation of tire spray and the complete splashing trajectory under a complex flow field are calculated by numerical simulations. Firstly, the initial patterns of tire water spray are simulated by the Smoothed Particle Hydrodynamics (SPH)-Finite Element (FE) coupling method in LS-DYNA software package, and the engine flow field is simulated in CFX software package. Secondly, the water spray particles information and engine flow field information are imported into a program to calculate the splashing trajectory under the influence of the complex flow field. In the process, the particles inhaled by the engine are counted, so the engine water inflow can be obtained under different working conditions and tire configurations, which can verify the suppression effect of the tire chine on the engine water inflow. Lastly, the complete splashing trajectory of the complex flow field simulated by the program is consistent with the result of the aircraft splash test, which proves the feasibility of the numerical simulation method for the complete splashing trajectory simulation.

© 2022 Elsevier Masson SAS. All rights reserved.

## 1. Introduction

When an aircraft passes through the contaminated runway, its tire water spray may affect the safety of the aircraft. The water spray generated by the landing gear may enter the inlet of the engine and affect the operation of the engine [1]. Therefore, the aircraft need to carry out the complete splash test in the airworthiness identification to ensure that there is no excessive water in the engine. If the engine water inflow does not meet the airworthiness standards, the tire configuration needs to be improved to suppress the water inflow of the engine, such as adding the chine or baffle to suppress water spray [2–4].

Considering the research cycle and the splash test cost of the whole aircraft, it is generally necessary to make an accurate estimate of the water spray patterns in the aircraft design stage, and the aircraft layout needs to be properly designed to avoid critical parts such as the engine affecting by tire water spray.

Therefore, many groups studied the numerical simulations of tire splash trajectory and the estimation of engine water inflow. In 1966, Langley Research Center studied the influence of tire load, aircraft speed and water accumulation depth on tire spray by using an array of tubes mounted behind the test tire [5–7]. At the same time, Barrett from Bristol University established a model test facility to study the tire spray. The process of the test method was to run the model wheel on an endless belt onto the surface, and a water film was ejected tangentially at the speed of the belt. In this way, the forward motion of a wheel on a fluid-covered runway was simulated [8–10].

In 1998, Engineering Sciences Data Unit (ESDU) proposed an engineering method to calculate the patterns of the side spray according to a large number of test results. According to the basic parameters such as tire parameters, depth of water accumulation and aircraft speed, the method calculated and described the parameters of side spray patterns, such as spray height, sputter angle, etc. However, the spray position was only roughly predicted, and the accuracy of this empirical model strongly depended upon the test data. If the selected parameters deviated from the value range of the formula, the error was large [11]. Besides, the method cannot predict the influence of spray suppression devices such as the spray deflector and the chine tire. In

\* Corresponding author at: Computational Marine Hydrodynamics Lab (CMHL), School of Naval Architecture, Ocean and Civil Engineering, Shanghai Jiao Tong University, Shanghai 200240, China.

E-mail address: [dcwan@sjtu.edu.cn](mailto:dcwan@sjtu.edu.cn) (D. Wan).

2003, Trapp and Oliveira simulated the effect of spattering on the EMB-170 aircraft thrust reversal device and got a spray pattern around the fuselage that fits well with the experimental photographs. However, they did not give specific numerical methods and quantitative results [12]. In 2013, the CR-SPRAY method using the Monte Carlo method was proposed by Gooden. According to the initial patterns of tire spray obtained by the ESDU method, the particle trajectory algorithm was used to calculate the complete splashing trajectory. This method could consider the influence of wind direction. At the same time, it also can calculate the wading resistance of tire spray, spray patterns and engine water inflow. However, the initial patterns were based on the empirical formulas from the ESDU, so the prediction results were still unreliable [13,14]. In 2012, ARJ21-700 first conducted the aircraft splash test, mainly studying the influence of tire water spray on the engine inlet. After that, Liu et al. used the Smoothed Particle Hydrodynamics (SPH) method to simulate the tire spray and the Discrete Phase Model (DPM) method to simulate the splashing trajectory in the software. They obtained the water spray patterns of the nose gear, which were in good agreement with the test results of ARJ21 [15–17]. Because of the limitation of software computing efficiency, the particle spacing was set too large (10 mm), which was not accurate for calculating the initial spray patterns of a tire. Accurate spatial distribution of water particles was also not available. Moreover, the determination of the droplet diameter was only based on a statistical result, and the influence of the droplet diameter was not analyzed. In the meantime, Xu et al. studied the water spray of an elastic large deformation tire by the SPH–FE coupling method and studied the phenomenon of tire hydroplaning [18–20]. They analyzed the influence of particle spacing to get accurate spray patterns and compared them with experimental results. They found that below 2 mm, the particle spacing had little effect on the spray patterns. However, they only got the initial spray patterns and the spatial distribution of water particles, not the complete splashing trajectory. Both of Liu and Xu used the FE method to simulate tires and the SPH method to simulate water films. The SPH method has been applied in much commercial software and has shown promising prospects in aircraft tire spray [21,22].

The main focus of the above study was the initial tire spray patterns and the subsequent splashing trajectory under the effect of the air flow field. In fact, the ground environment is complex in the process of aircraft take-off and landing. In addition to the influence of the crosswind and air flow field, the engine will produce a strong flow field disturbance near its inlet. Some splashing droplets will be inhaled by the engine, causing hidden dangers to the regular operation of the engine. However, since the calculation time of the complete splashing trajectory was too long, the influence of the engine flow field on the spray patterns and the engine water inflow was less studied.

Tire spray belongs to Fluid–structure Interaction (FSI) problem, and many violent FSI problems involve some non-negligible coupling effects due to the presence of strong reciprocal interactions. The finite element method (FEM) is classically used for structure modeling [17,18], but the grid method does not dominate in the numerical simulation of water films. Although the grid method has successfully solved many flow problems, there are still many difficulties in the simulation of tire spray problems. In the tire splashing process, the tire impacts the water film in a short time. The water film will quickly deform, break, and then spray out. The traditional mesh method has difficulties in calculating the free surface boundary, deformation of boundary and moving interface flow of the liquid. Because the traditional grid method usually needs to use dynamic grid technology or nested grid technology to control the change of the grid, when the boundary deformation is large, the grid distortion problem

is often encountered. The distorted mesh seriously reduces the calculation accuracy and even causes the calculation divergence. Although the finite volume method (FVM) with a volume-of-fluid (VOF) can deal with the flow of liquid, the free-surface capture of water breaking is difficult due to the sharp change of liquid in a short period [23].

The meshless method obtains accurate and stable numerical solutions using a series of arbitrarily distributed nodes (or particles) to solve integral equations or partial differential equations (PDEs) with different boundary conditions [24,25]. These nodes (or particles) do not require mesh connections, which can easily solve the large deformation, moving interface and free surface problems encountered during numerical simulation [26,27]. SPH method is one of the popular meshless methods. The SPH method could avoid the precision damage caused by mesh distortion when extremely large deformation appears, and it would be flexible by using the SPH method in dealing with the large deformation and breaking of liquid. The SPH method has been widely used in many practical problems [28,29], such as incompressible flow, explosion shock, high-speed compressible flow, underwater explosion, free surface flow, fluid–structure interactions, etc. Though entirely Lagrangian meshfree computational methods for hydroelastic fluid–structure interactions have made a lot of progress [30,31], the simulation of elastic structures is limited to simple geometric structures. If the elastic structure is complex, the SPH method is generally coupled with the FE method to deal with fluid–structure interactions. Since both the SPH method and the FEM are methods with a Lagrangian viewpoint, the coupling of the SPH method and the FEM can easily simulate the free surface liquid flow interacting with the deformed structure. In addition to Liu and Xu's study, Li used the SPH–FEM method to simulate transient FSI problems even in the presence of large interface motion, which ensured a zero algorithmic interface energy and synchronized time integration of each sub-domain. Finally, a 3-D tire hydroplaning example showed the feasibility of the proposed method for more industrial multi-dimensional problems with complicated interface geometry [32]. Oger also used the SPH–FE coupling method to simulate the hydroplaning phenomenon of a car tire. A new algorithm dedicated to such SPH–FE coupling strategy was proposed to optimize the computational efficiency through the use of differed time steps between fluid and solid solvers [33]. The spacing of the particles was fine (0.25 mm), so the simulation of the tire hydroplaning phenomenon was accurate. However, they did not study the tire spray patterns. Their study demonstrated the effectiveness of the SPH–FE coupling method in simulating the tire spray problem. Based on the previous research, we decided to use the SPH–FE coupling method to simulate the tire water spray.

Both Xu and Liu [15,18] established a tire spray model and carried out a numerical simulation of tire spray in LS-DYNA software package. Because LS-DYNA enables coupling the SPH method with the finite element method (FEM), having mutual advantages in structural dynamics and large deformation. The numerical simulations of fluid–structure interaction (FSI) are carried out with fluid modeled with smoothed particles. The convergence verification of the SPH–FE coupling strategy in LS-DYNA was also studied. Pelfrene (2011) studied the dam break case, using the SPH in LS-DYNA to validate the conservative properties of mass and volume. It was found that the SPH solver in LS-DYNA was able to simulate laminar free surface flow and to capture the main features of plunging breaking waves. The results indicated that weakly compressible SPH (WCSPH) of LS-DYNA was characterized by the preservation of linear/angular momenta similar to other WCSPH schemes [34]. Lee and Hong studied the optimal parameters for the fluid–structure interaction analysis using the SPH particles for fluids and finite elements

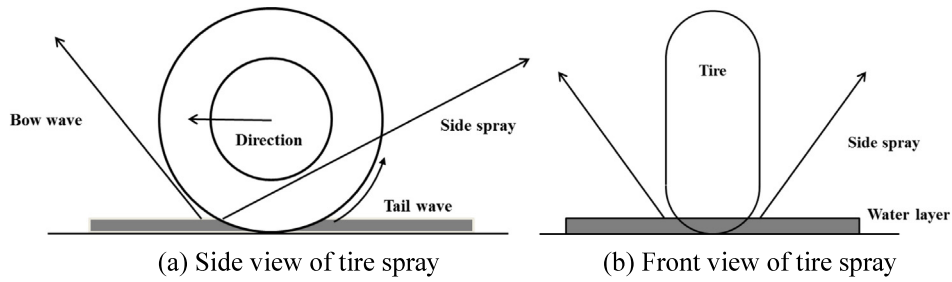


Fig. 1. The sketches of tire water spray.

for structures in LS-DYNA. The effectiveness of the simulations with those parameters was validated by solving a dam-break problem and an elastic plate deflection problem, which proved the SPH-FE coupled simulation was very effective in calculating the fluid-structure interaction [35]. Meanwhile, Lee used the SPH-FE coupling method to build a numerical wave tank model. The numerical wave parameters were in good agreement with the experimental results, and the study verified the accuracy of the SPH-FE coupling method in LS-DYNA [36].

This paper proposes a more efficient and accurate calculation method for simulating the complete splashing trajectory in the complex flow field. Compared with the previous methods, this method can significantly reduce the calculation time, and the calculation accuracy is guaranteed. Firstly, the initial spray patterns of an elastic pneumatic tire are first obtained by the SPH-FE coupling method in LS-DYNA software package [18], and the position and velocity information of the splashing particles is exported. Secondly, the flow field of the aircraft engine when operating on the ground is simulated in CFX, and the flow field information around the engine is exported. Finally, a program is written in MATLAB to simulate the subsequent splashing trajectory under the engine flow field. The feasibility of the method is verified by comparing the simulated splashing trajectory with the result of the aircraft splash test. At the same time, the engine water inflow under different working conditions and tire configurations is also obtained.

## 2. Simulation of initial spray patterns

### 2.1. The model of tire spray

The phenomenon of tire spray belongs to a typical shallow water impact problem. The tire squeezes the water film during the wading process, and the water film is deformed under pressure, which leads to the water film breaking and liquid droplets splashing. The tire spray is formed after a series of complex processes such as droplet collision and convergence. The tire spray is mainly divided into three parts: bow wave and side spray and tail wave. The bow wave is splashed from the front of tires, and the side spray is splashed from the sides of tires. The viscosity force makes a small amount of water adhere to the tread as the tire turns back for a time, forming the tail wave. The sketches of tire spray are shown in Fig. 1.

In this paper, the finite element model of a tire is established in Hypermesh based on the data of a specific type of aircraft tire and imported into LS-DYNA. The actual tire configuration is very complex, composed of tread, belt layer, side wall, wire coil, inner tube, tire curtain layer and tire hub. The tire spray patterns are only related to the shape and deformation of the tire, so the tire model is simplified, only including the tread, side wall, inner tire, rim (a simplified version of the hub) and chine, as shown in Fig. 2. The chine is only added to one side of the tire. The tread, sidewall and chine are made of Mooney-Rivlin material.

Mooney-Rivlin material is a kind of hyperelastic material, which is usually used to simulate rubber. The inner tube is made of elastic material, and the rim is made of rigid material. A force (22 kN) is applied to the rim to simulate the load on the tire, and the velocity boundary condition is set according to the working condition. A uniformly distributed pressure of 0.62 MPa is applied to the normal direction of the inner tire surface to simulate the tire pressure of a pneumatic tire. The tire is the front wheel of ARJ21, and the data of the tire is provided by the Commercial Aircraft Corporation of China Ltd.

### 2.2. Numerical method

The SPH method is an N-body integration scheme, which avoids the limitations of mesh tangling encountered in large deformation problems with the FEM. The main difference between the SPH method and traditional mesh methods is the absence of the grid. Therefore, the particles are the computational framework on which the governing equations are resolved. We quoted the relevant SPH formulas as they are implemented in LS-DYNA [37].

The particle approximation of a function is written as:

$$\prod f(\mathbf{x}_i) = \sum_{j=1}^N w_j f(\mathbf{x}_j) W(\mathbf{x}_i - \mathbf{x}_j, h) \quad (2.1)$$

where  $W$  is the kernel function, subscripts  $i$  and  $j$  are particle labels,  $N$  is the number of particles in the influence domain of particle  $i$ ,  $w_j = \frac{m_j}{\rho_j}$  is the volume of the particle,  $\mathbf{x}$  is the coordinate of particle,  $h$  is the smoothing length,  $m$  is the mass of the particle, and  $\rho$  is the density.

The most common smoothing kernel used by the SPH community is the cubic B-spline, which is defined as [37]:

$$W(\mathbf{x}_i - \mathbf{x}_j, h) = C \begin{cases} 1 - \frac{3}{2}u^2 + \frac{3}{4}u^3 & u \leq 1 \\ \frac{1}{4}(2 - u)^3 & 1 < u \leq 2 \\ 0 & u > 2 \end{cases} \quad (2.2)$$

where  $u = \frac{\|\mathbf{x}_i - \mathbf{x}_j\|}{h}$ ,  $C$  is a constant of normalization that depends on the number of space dimensions. If the number of space dimensions is 3,  $C$  is  $\frac{1}{\pi h^3}$ .

The continuity equation, moment equation, and energy equation are:

$$\frac{d\rho}{dt} = -\rho \frac{\partial v^\beta}{\partial x^\beta} \quad (2.3)$$

$$\frac{dv^\alpha}{dt} = \frac{1}{\rho} \frac{\partial \sigma^{\alpha\beta}}{\partial x^\beta} + F^\alpha \quad (2.4)$$

$$\frac{de}{dt} - \frac{\sigma^{\alpha\beta}}{\rho} \frac{\partial v^\alpha}{\partial x^\beta} = 0 \quad (2.5)$$

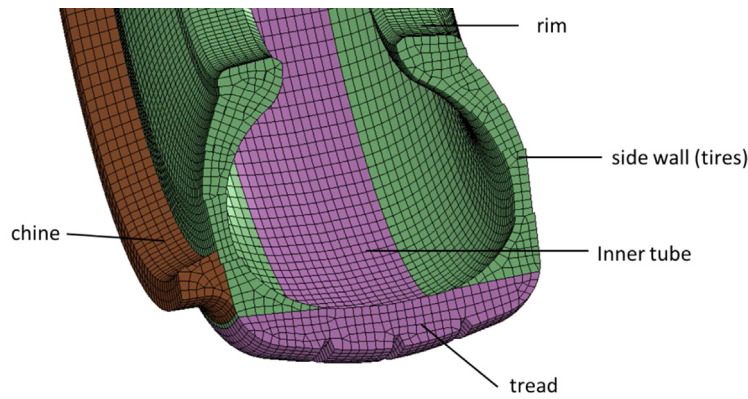


Fig. 2. Tire configuration.

where the superscripts  $\alpha$  and  $\beta$  are the space indices ( $\{x, y, z\}$ ),  $x^\beta$  are the coordinates,  $v^\alpha$  are the velocities,  $F^\alpha$  is the body force,  $e$  is the internal energy,  $\sigma^{\alpha\beta}$  are the total stresses, and  $t$  is the time.

The discrete forms of momentum conservation equation and energy conservation equation in the SPH method are:

$$\frac{d\rho_i}{dt} = \sum_{j=1}^N m_j (v_i^\beta - v_j^\beta) \frac{\partial W_{ij}}{\partial x_i^\beta} \quad (2.6)$$

$$\frac{dv_i^\alpha}{dt} = \sum_{j=1}^N m_j \left( \frac{\sigma_i^{\alpha\beta}}{\rho_i^2} + \frac{\sigma_j^{\alpha\beta}}{\rho_j^2} \right) \frac{\partial W_{ij}}{\partial x_i^\beta} + F_i^\alpha \quad (2.7)$$

$$\frac{de_i}{dt} = -\frac{1}{2} \sum_{j=1}^N m_j \left( \frac{\sigma_i^{\alpha\beta}}{\rho_i^2} + \frac{\sigma_j^{\alpha\beta}}{\rho_j^2} \right) (v_i^\beta - v_j^\beta) \frac{\partial W_{ij}}{\partial x_i^\beta} \quad (2.8)$$

$$\sigma^{\alpha\beta} = -p\delta^{\alpha\beta} + \tau^{\alpha\beta} \quad (2.9)$$

For Newtonian fluids, deviatoric stress can be defined as:

$$\tau^{\alpha\beta} = 2\mu\dot{\varepsilon}^{\alpha\beta} \quad (2.10)$$

where  $\tau^{\alpha\beta}$  are the viscous stresses,  $\dot{\varepsilon}^{\alpha\beta}$  are the shear strain rates,  $p$  is the isotropic pressure, and  $\mu$  is the shear viscosity of the fluid.

If we add the artificial viscosity, Eq. (2.7) can lead to the following equation.

$$\frac{dv_i^\alpha}{dt} = \sum_{j=1}^N m_j \left( \frac{\sigma_i^{\alpha\beta}}{\rho_i^2} + \frac{\sigma_j^{\alpha\beta}}{\rho_j^2} + \prod_{ij} \right) \frac{\partial W_{ij}}{\partial x_i^\beta} + F_i^\alpha \quad (2.11)$$

To take into account the artificial viscosity, an artificial viscous pressure term  $\prod_{ij}$  is added such that [38]:

$$\prod_{ij} = \frac{1}{\rho_{ij}} (-A\mu_{ij}\bar{c}_{ij} + D\mu_{ij}^2) \quad (2.12)$$

$$\mu_{ij} = \begin{cases} \frac{\bar{h}_{ij}}{|\mathbf{r}_{ij}|^2 + \eta^2} \frac{\mathbf{v}_{ij} \cdot \mathbf{r}_{ij}}{|\mathbf{r}_{ij}|} & \text{if } \mathbf{v}_{ij} \cdot \mathbf{r}_{ij} < 0 \\ 0 & \text{otherwise} \end{cases} \quad (2.13)$$

where  $\mathbf{v}_{ij} = (\mathbf{v}_i - \mathbf{v}_j)$ ,  $\mathbf{r}_{ij} = (\mathbf{r}_i - \mathbf{r}_j)$ ,  $\eta^2 = 0.01\bar{h}_{ij}$ ,  $\bar{\rho}_{ij} = 0.5(\rho_i + \rho_j)$ ,  $\bar{h}_{ij} = 0.5(h_i + h_j)$ ,  $\bar{c}_{ij} = 0.5(c_i + c_j)$ ,  $A$  and  $D$  are the constants,  $A$  is 0.06,  $D$  is 1.5, and  $c$  is the adiabatic sound speed.

We use a classical and straightforward first-order scheme for integration. The time step is determined by the expression:

$$\delta t = C_{CFL} \text{Min}_i \left( \frac{h_i}{c_i + v_i} \right) \quad (2.14)$$

where the factor  $C_{CFL}$  (Courant–Friedrichs–Lewy) is a numerical constant. The  $C_{CFL}$  in the paper is 0.5.

Table 1

State equation parameters and material parameters of water.

GRUNISEN function	C (m/s)	S <sub>1</sub>	S <sub>2</sub>	S <sub>3</sub>	γ <sub>0</sub>	a
	1480	2.16	-1.985	0.2268	0.5	2.67
Null		ρ <sub>0</sub> (kg/m <sup>3</sup> )		Mu (kg/(m s))		
		1000		0.00768		

The material property of water is simulated by combining a NULL material with a Gruneisen equation of state, which uses a cubic shock velocity and fluid particle velocity to determine the pressure of compressed and expanded water [18]. The parameters are shown in Table 1

The Gruneisen equation of state with cubic shock velocity-particle velocity defines pressure for water as [18,35,39]:

$$p = \frac{\rho_0 B^2 k \left[ 1 + \left( 1 - \frac{\gamma_0}{2} \right) k - \frac{a}{2} k^2 \right]}{1 - (S_1 - 1)k - S_2 \frac{k^2}{k+1} - S_3 \frac{k^3}{(k+1)^2}} + (\gamma_0 + ak) E \quad (2.15)$$

where  $\rho_0$  is the initial density,  $B$  is the intercept of the shock velocity-particle velocity curve,  $S_1$ ,  $S_2$  and  $S_3$  are the coefficients of the slope of the shock velocity-particle velocity curve,  $\gamma_0$  is the Gruneisen gamma, and  $a$  is the first order volume correction to  $\gamma_0$ . The compression  $k$  is defined in terms of the relative volume  $V$  as:  $k = \frac{1}{V} - 1$ . The relative volume  $V$  is  $\frac{\rho_0}{\rho}$ .

The particle spacing of the water model is set to 2 mm, then the convergence of the particle spacing and the accuracy of the tire spray model was verified [18,20]. The geometric parameters of the water film are as follows: 400 mm width (in the X direction), 800 mm length (in the Y direction length), and 16 mm depth (in the Z direction). The total number of particles is 640 000. The tire spray model is shown in Fig. 3. The total number of the tire grids is 124,320.

The SPH–FE coupling strategy is partitioned coupling. The SPH particles are designated as a slave part and finite element as a master part using the node-to-surface contact algorithm. A reactive force proportional to the penetration force is applied, which uses the penalty-based contact algorithm to prevent the penetration phenomenon and form a contact interface between the structure and the particle. The calculation time steps for finite element and smoothed particles are determined based on the CFL condition, and the constant time step scale factor  $\beta$  is multiplied to the minimum time step for stable calculation. The scale factor  $\beta$  is set to a default value of 0.9 [36].

### 2.3. Initial tire spray patterns

After the numerical simulation of the tire spray is completed, the calculation results are obtained. Since the aircraft fuselage

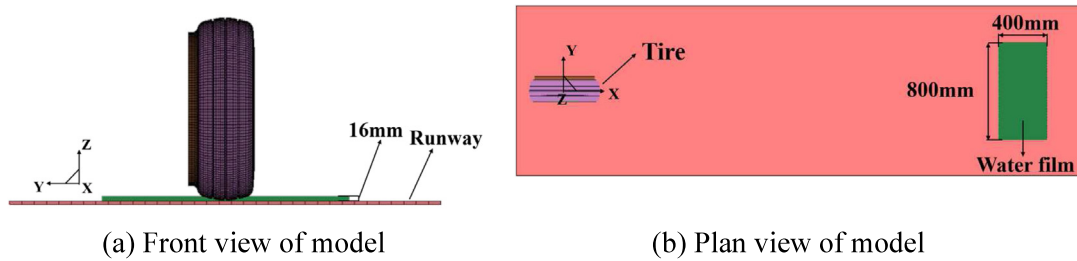


Fig. 3. The model of tire water spray.

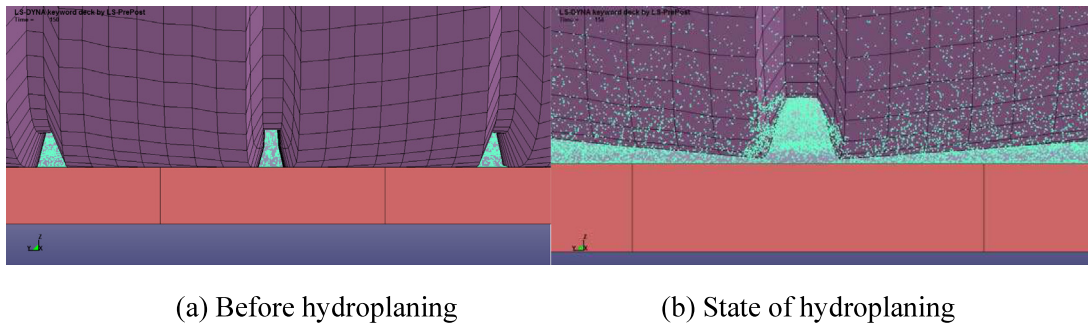


Fig. 4. Schematic of hydroplaning phenomenon.

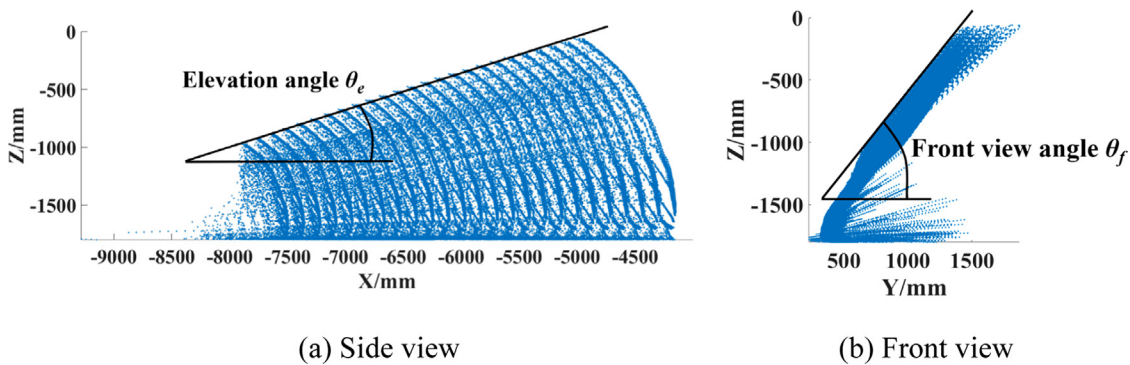


Fig. 5. Initial tire spray patterns.

will block the bow and tail waves, the tire water spray is composed of side spray. The position and velocity information of the side spray particles is exported.

When the tire slides through the water film, it will receive the dynamic pressure generated by water. The dynamic pressure of water is positively correlated with the speed square. When the dynamic pressure and the tire pressure are balanced, the tire is completely detached from the ground. The tire will slide over the water film, which is called the hydroplaning phenomenon of the tire, as shown in Fig. 4. The sliding speed is the hydroplaning speed of the tire, which is positively related to the tire pressure. The relationship is  $V = 108.5p^{0.5}$  knots (The unit of pressure is Mpa, and the unit of velocity is knot), so the hydroplaning speed of the tire in this calculation is 89 knots. The tire will slide over the water film when the sliding speed exceeds hydroplaning speed. The tire will be raised, and the tire wading depth will be reduced.

Due to the limitation of calculation ability and the requirement of calculation accuracy, the length of the water film in the forward direction is only 200 mm, and the wading time of the tire is only 6 ms. Therefore, the tire spray cannot form a spray pattern with a stable elevation angle at the same time in the numerical simulation. According to the relationship between the tire speed and the

time interval, the particles at different times are superimposed to form a relatively stable pattern of spray, which is the initial water spray pattern. The parameters of spray patterns are front view angle ( $\theta_f$ ) and elevation angle ( $\theta_e$ ), which are shown in Fig. 5. The parameters of spray patterns under different working conditions are shown in Fig. 6.

According to Fig. 6, we can obtain that the front view angle and elevation angle increase first and then decrease with the tire speed. The elevation angle is maximum at 90 knots, and the front view angle is maximum at 110 knots. After the water particles splash, the X-axis velocity is consistent with the direction of the tire sliding velocity and slightly smaller than tire sliding speed, so the elevation angle is mainly determined by the velocity of the vertical direction of the splashing particles (in the Z direction).

The tire will slide over the water film when the sliding speed exceeds hydroplaning speed. The tire will be raised, and the tire wading depth will be reduced. As a result, the Z-direction velocity of splashing particles decreases accordingly, resulting in the elevation angle and the front view angle decreasing. At the same time, due to the hydroplaning phenomenon, the tire's height will also be correspondingly improved, which results in a reduced suppression of the chine on tire spray. Therefore, when the tire sliding speed exceeds 90 knots, the difference between

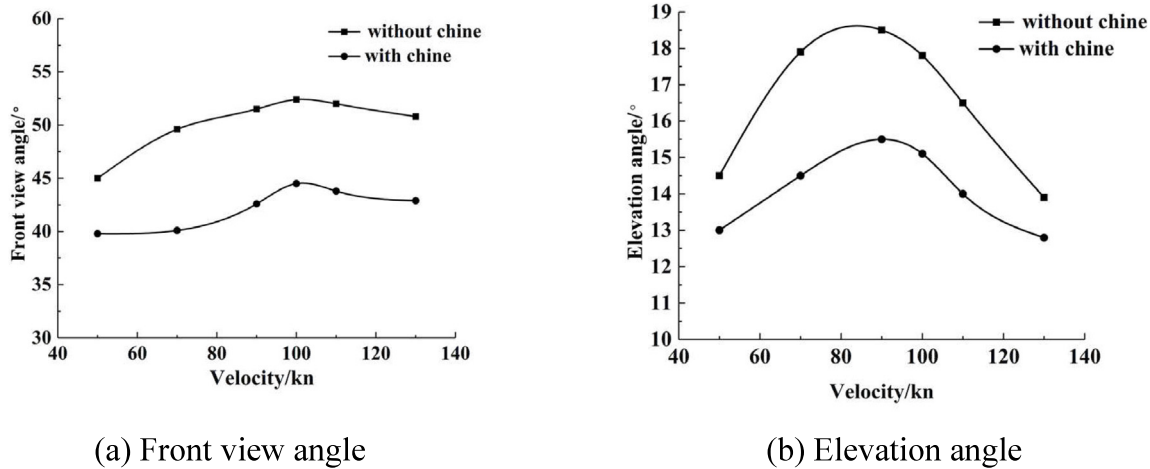


Fig. 6. The angles of tire spray under different conditions.

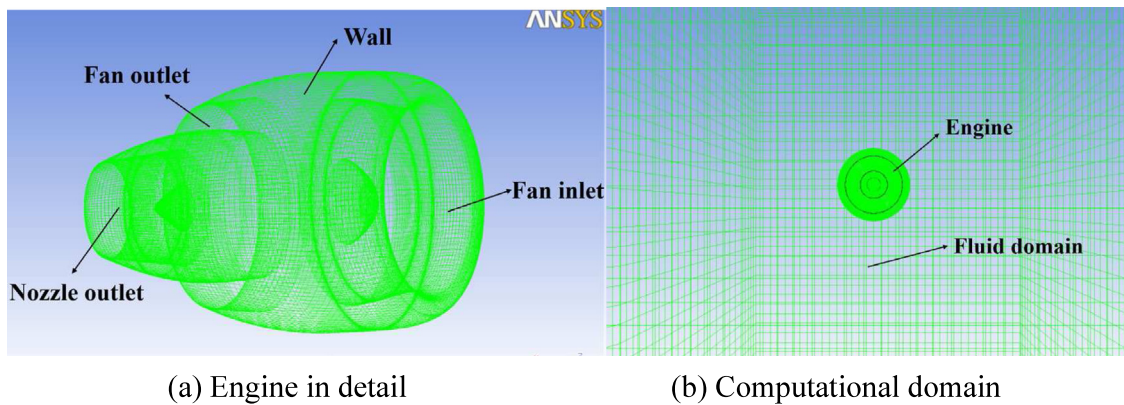


Fig. 7. Schematic diagram of the engine model.

the spray angle of the tire with chine and that of the tire without chine is smaller.

### 3. Simulation of splashing trajectory under complex flow field

#### 3.1. Simulation of engine flow field

The engine model is built in ICEM CFD, whose geometric parameters are according to the size of the ARJ21 engine. ICEM-CFD is used to generate the mesh of the computational domain. The computed domain range is 20 m \* 20 m. In order to calculate the flow field near the engine accurately, the grids around the engine wall, the engine inlet and the culvert outlet are more intensive. The total number of grids is 5.61 million, and the model is shown in Fig. 7.

The established engine model is imported into CFX, where the fluid domain parameters and boundary conditions are set. CFX is a computational fluid dynamics software that uses the finite volume method. The medium of the flow field domain is set to the ideal gas, the heat transfer calculation is set to the Total Energy mode, the calculation of turbulence is set to the Shear stress transport mode, and the velocity of the flow field is set to the aircraft velocity. The boundary conditions mainly include flow field inlet, fan inlet, fan outlet, nozzle outlet and flow field outlet. By consulting the relevant information, the boundary conditions of the engine in the take-off state are shown in Table 2.

The simulation results of the engine flow field are shown in Fig. 8. Regardless of the flow field near the engine outlet, if the distance from the engine center exceeds 5 m, the velocity

Table 2

Boundary parameters of engine and fluid domain.

Boundary	Boundary	Pressure(relative)	
Fan inlet	Outlet	-23543 Pa	
	Boundary	Pressure(relative)	Temperature
Fan outlet	Inlet	58687 Pa	348 K
Nozzle outlet	Inlet	42641 Pa	865 K
Flow field inlet	Inlet	0 Pa	298 K
Flow field outlet	Outlet	0 Pa	298 K

and pressure of this position are unchanged, which is similar to the air flow field. Therefore, the center of the engine inlet is first determined as the sphere center, then the sphere region with a radius of 5 m is selected. Finally, the information of flow field position, velocity and pressure gradient within this region is exported.

#### 3.2. Calculation method of droplet trajectory under complex flow field

Fig. 9 is the velocity curve of the splashing particles in LS-DYNA, and the calculation of the particles is not affected by air. The SPH particles can simulate the deformation, fragmentation, and fusion of liquid droplets, which connect each other by force determined by the kernel function. If the distance between particles is beyond the scope, the force between particles can be ignored. It can be seen from Fig. 9 that the velocity of the particles remains relatively stable after the particles form a side

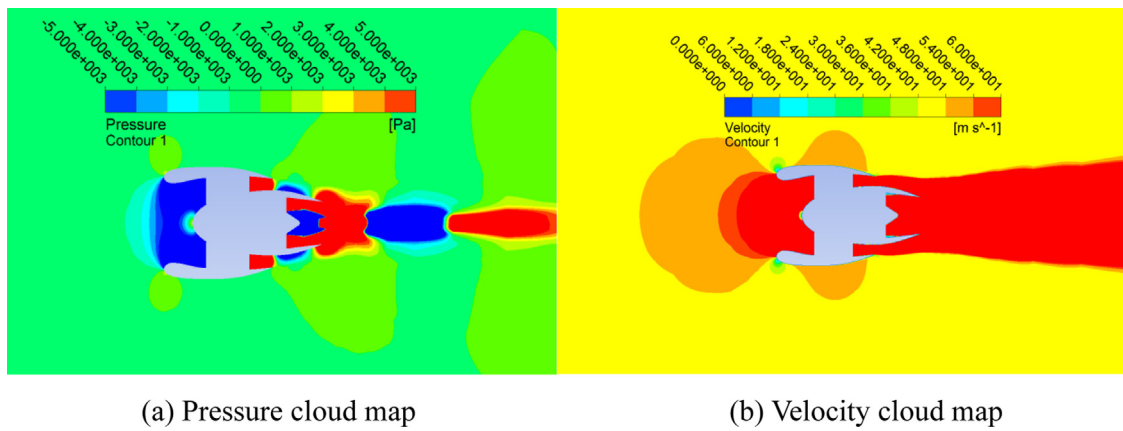


Fig. 8. Simulation results of the engine flow field.

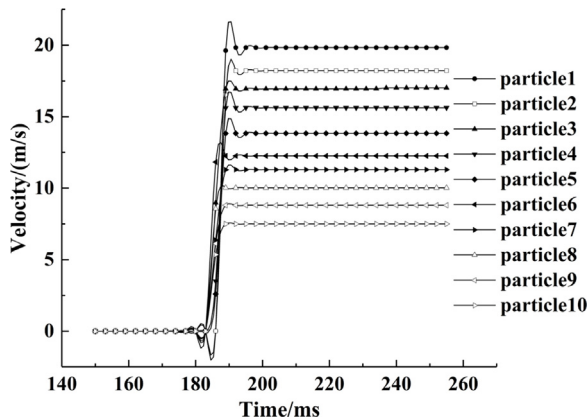


Fig. 9. Velocity curve of the splashing particles.

spray pattern. That shows that once the particles are dispersed, the force between the particles is negligible, and the motion of splashing particles will be affected by flow field and gravity.

The air resistance of the water particles in the engine flow field is:

$$F = \frac{1}{2} \rho v^2 A C_d \quad (3.1)$$

where  $A$  is the cross-sectional area of the droplets,  $A = \frac{\pi d^2}{4}$ ,  $d$  is the diameter of the droplet, and  $C_d$  is the air resistance coefficient.

The Reynolds number  $Re$  and the resistance coefficient  $C_d$  are calculated as follows [40]

$$Re = \frac{\rho v d}{\mu} \quad (3.2)$$

$$C_d = \begin{cases} \frac{24}{Re} (1 + 0.15 Re^{0.681}) + \frac{0.407}{1 + 8710 Re^{-1}} & Re \leq 1000 \\ 0.44 & Re > 1000 \end{cases} \quad (3.3)$$

The droplets are much smaller than the spatial scale of the pressure gradient field, so they can be treated as particles.

The acceleration of the particle is calculated as follows:

$$\frac{dv^\alpha}{dt} = -\frac{3}{4} \frac{\rho_a}{\rho_w} \frac{C_d}{d} |v| v^\alpha - \frac{1}{\rho_w} \frac{\partial p}{\partial x^\alpha} + g^\alpha \quad (3.4)$$

where the superscript  $\alpha$  still represents the space indices ( $\{x, y, z\}$ ),  $g^\alpha$  is the gravity,  $\rho_a$  is the air density,  $\rho_w$  is the water density, and  $p$  is the flow field pressure.

A program is written in MATLAB to calculate the subsequent trajectory of the tire spray under the influence of the engine flow field.

In the paper, the splashing trajectory of the nose gear is calculated, and the coordinates of the initial spray position relative to the engine are  $(-18 \text{ m}, 2.5 \text{ m}, 2.8 \text{ m})$ . In order to eliminate the influence of high-pressure and high-speed flow fields at the engine outlet, the engine flow field is modified. The flow field behind the engine outlet is deleted and replaced by an air flow field. As shown in Fig. 10, the front view angle of the spray exceeds 60 degrees before the spray hits the fuselage. According to the calculated initial spray patterns, the front view angles under different working conditions are less than 60 degrees, so the fuselage will not block the spray. Therefore, the boundary condition of the fuselage is not added in MATLAB. Only the boundary condition of the wing and engine are added. The splashing particles below the wing will be blocked by the wing and deleted.

As shown in Fig. 10(b), the angle between the nose gear and the engine upper edge is 12.5 degrees. The angle between the nose gear and the engine center is 11.7 degree. The angle between the nose gear and the wing upper edge is 10.8 degrees. These angles will be mentioned in the following discussion on elevation angle.

The specific calculation processes are as follows:

- (1) The information of the initial water spray, engine flow field and boundary conditions are imported into the program.
- (2) Calculation time is determined according to the sliding speed of the aircraft. At each time step, loops are established based on the number of particles.
- (3) Each particle is regarded as a droplet, and the physical quantity of the droplet is imported. Each droplet's position information is first read, and then its corresponding flow field information is determined. If the distance between the droplet position and the center of the engine flow field is more than 5 m, the flow field is considered the air flow field. The velocity is the crosswind velocity, the pressure gradient is 0, and the density is  $1.29 \text{ kg/m}^3$ . If the distance is less than 5 m, the search domain gradually increases. If the engine flow field information is present in the search domain, the acquired flow field information is averaged, and the search is stopped.
- (4) The velocity of the droplet relative to the flow field is determined. The droplet's Reynolds number and air resistance coefficient are determined based on the velocity. According to the equation, the external forces on the droplet are calculated, including air resistance, pressure gradient force and gravity. Then the acceleration of the droplet can be

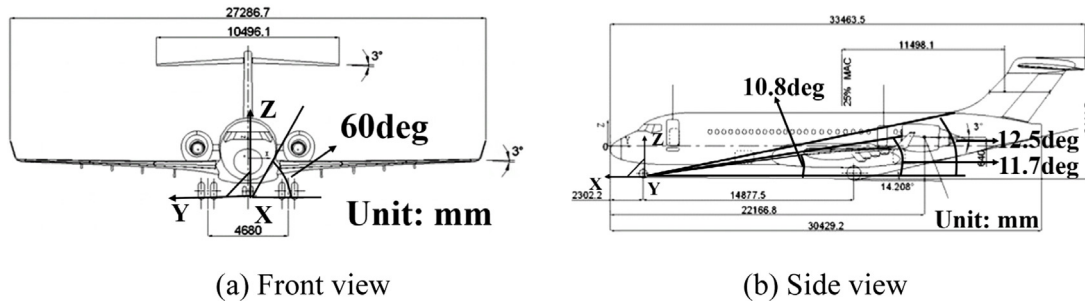


Fig. 10. Aircraft geometry diagrams.

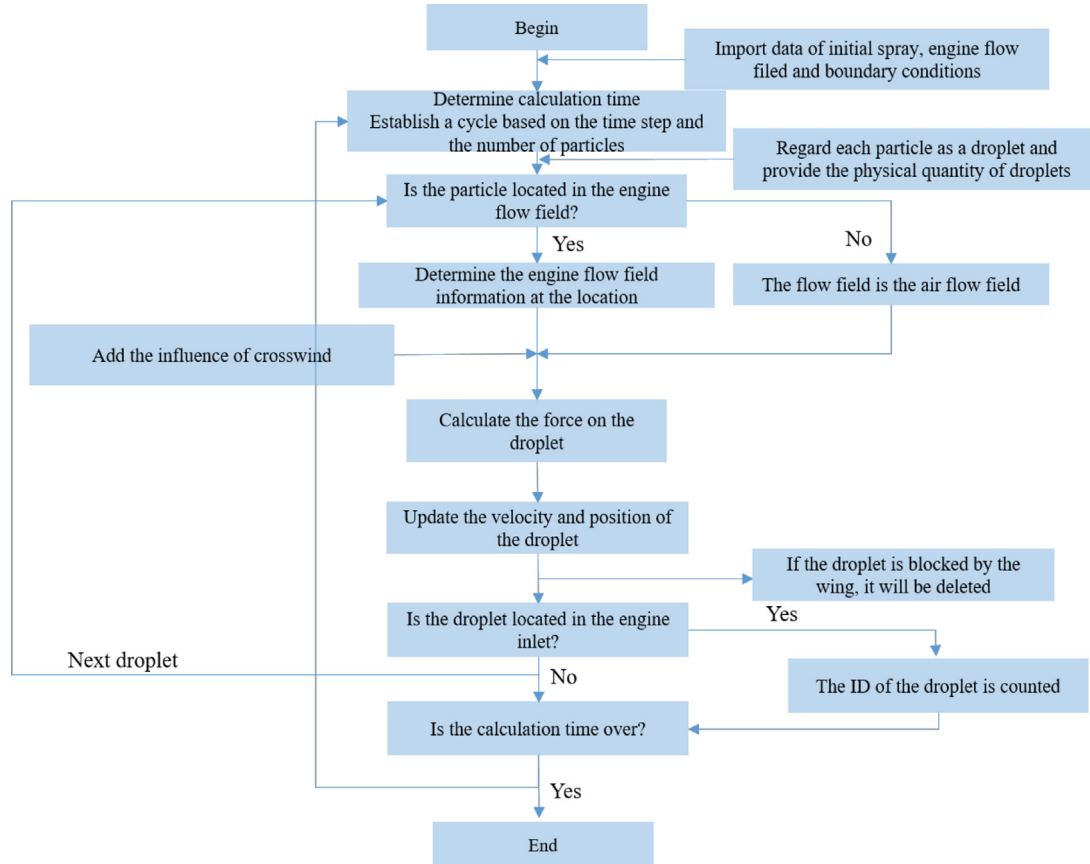


Fig. 11. Flow chart of the droplet's trajectory calculation.

obtained, which makes the velocity and position information of the droplet updated. If the droplet is blocked by the wing, it will be deleted.

- (5) According to the droplet's position, the droplet's ID at the engine inlet is counted, and the water inflow of the engine is obtained.
- (6) After each step is completed, the engine flow field, engine position and wing position information are updated according to the aircraft speed. Meanwhile, the droplet position information at this step is retained (see Fig. 11).

### 3.3. Determination of droplet diameter

The size of SPH particles in LS-DYNA is 2 mm, which is determined according to the convergence and efficiency of calculation. It represents the spacing of SPH particles, not the radius of droplets. The information of the initial spray only includes

the velocity and position of droplets, not the size of droplets. The droplets have different sizes in the flow field, and the drag coefficient of droplets in the complex flow field also depends on the size, so the average size of droplets should be determined first. NASA gives the distribution of droplet diameter based on experiments [13]. As shown in Fig. 12, four positions at different distances from the nose gear are selected for the test. The splashing water at these positions is collected, which is analyzed to obtain the droplets size distribution at these four different positions. The distance between the engine and the nose gear is about 16 m. According to Fig. 12, when the distance is 12.8 m, the diameter of the most concentrated splashing droplets is 2 mm. Therefore, the diameter of droplets is assumed to be 2 mm in the subsequent splashing trajectory simulation. In addition to the results of NASA, the comparison between the experimental results and the simulation results can also determine the droplet size. The same initial spray pattern is selected, and then the splashing trajectories under different droplet sizes (droplet diameters are

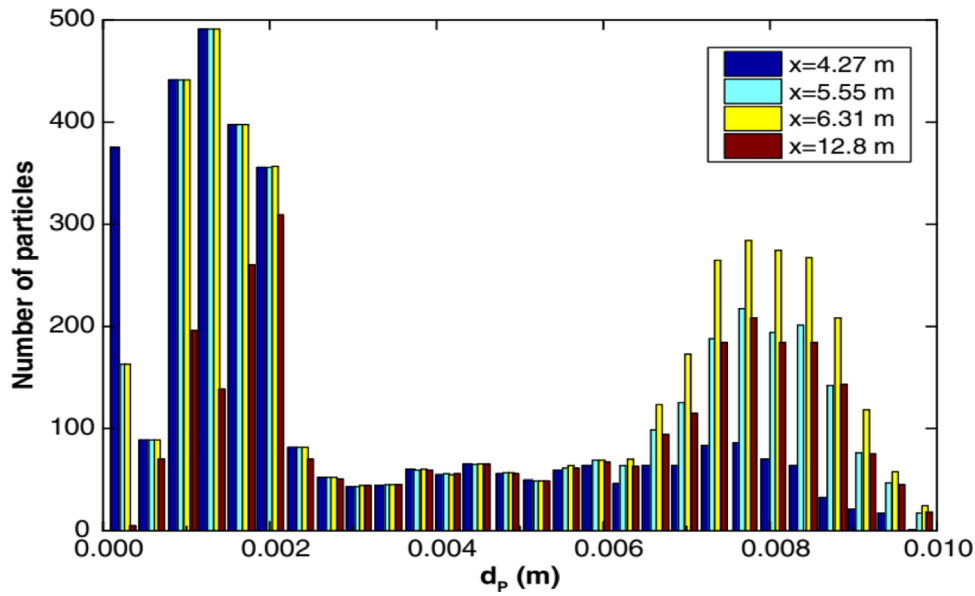


Fig. 12. Distribution of the splashing droplets diameter.

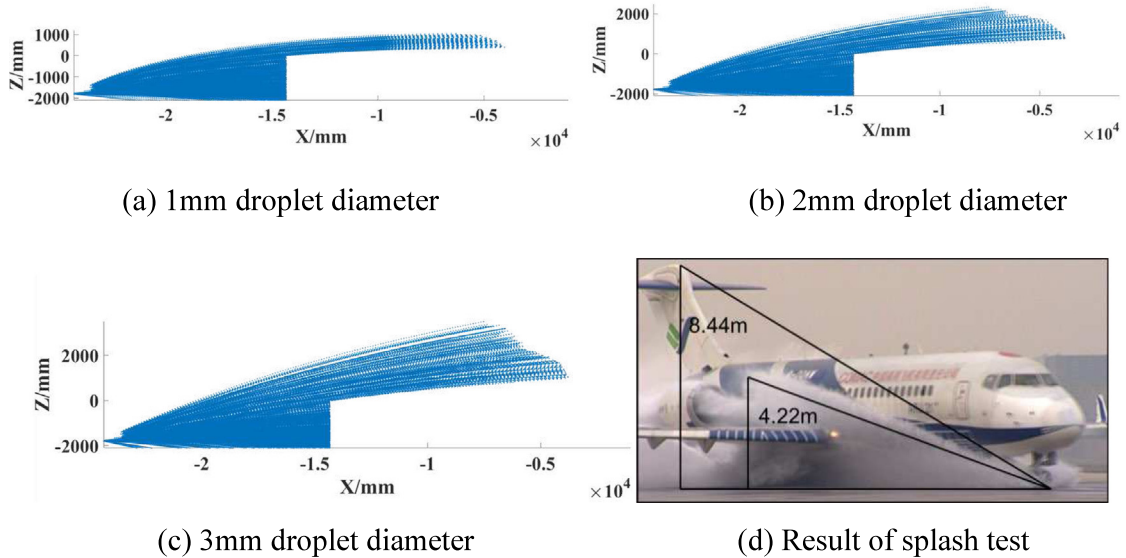


Fig. 13. Comparison between simulation results and test result.

1 mm, 2 mm and 3 mm) are simulated and calculated in the engine flow field. The splashing trajectories are shown in Fig. 13.

The result of the tire splash test under the same condition is shown in Fig. 13(d). The splashing height of the splash test is 4.22 m, which is very consistent with the simulated splashing trajectory under 2 mm droplet diameter. Therefore, the 2 mm droplet diameter is uniformly used for the calculation of the splashing trajectory. At the same time, the size of particles in LS-DYNA is also 2 mm, which is just consistent with the diameter of droplets.

#### 4. Discussion of simulation results

##### 4.1. Tire spray patterns under the influence of engine

Under the condition of 90 knots and 16 mm water depth, the splashing trajectory of the tire without chine under the influence of the complex flow field is shown in Fig. 14. The splashing trajectory in Fig. 14(a) only considers the influence of air flow field and

gravity. The splashing trajectory in Fig. 14(b) also considers the influence of the engine flow field. Considering that the elevation angle of the splashing trajectory gradually decreases under the influence of air and gravity, the angle between the splashing trajectory above the wing and the initial point of spray is selected as the elevation angle of the spray pattern, as shown in Fig. 14.

The marked part in Fig. 14(b) is the area obviously affected by the engine flow field. Therefore, it can be seen that the splashing trajectory near this position is obviously sucked in. Under this working condition, the elevation angle of spray is reduced due to the engine flow field. The influence of engine flow field on spray patterns under different working conditions is shown in Table 3. The parameters of Table 3 are front view angle ( $\theta_f$ ) and elevation angle ( $\theta_e$ ). The results on the left side of the table are the results without considering the engine flow field, and the results on the right side are the results considering the engine flow field.

It can be seen from Table 3 that the engine flow field has a little influence on the elevation angle of spray but has little influence on the front view angle. The axial velocity (X direction)

**Table 3**  
Patterns of tire spray under different conditions.

Conditions	$\theta_e$ (without chine)	$\theta_e$ (with chine)	$\theta_f$ (without chine)	$\theta_f$ (with chine)
50 kn	12.7/12.1	10.8/11.3	45/45.1	39.8/39.8
70 kn	14.3/14.2	12.5/12.3	49.6/49.6	40.1/40.1
90 kn	14.6/14.5	13.8/13.7	51.5/51.6	42.6/42.6
110 kn	13.7/13.5	13.4/13.2	52/51.9	45/45
130 kn	12.3/11.7	11.7/11.9	50.8/50.8	43.3/43.3

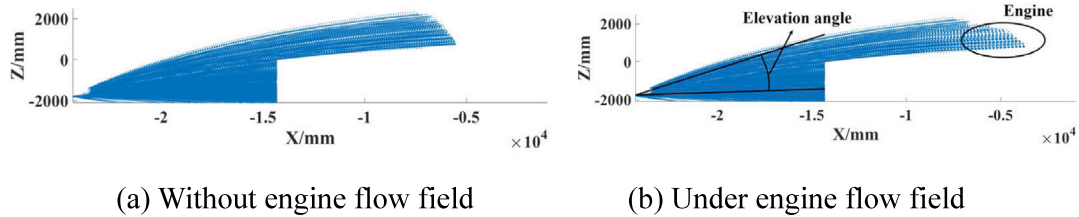


Fig. 14. Splashing trajectory of tire spray.

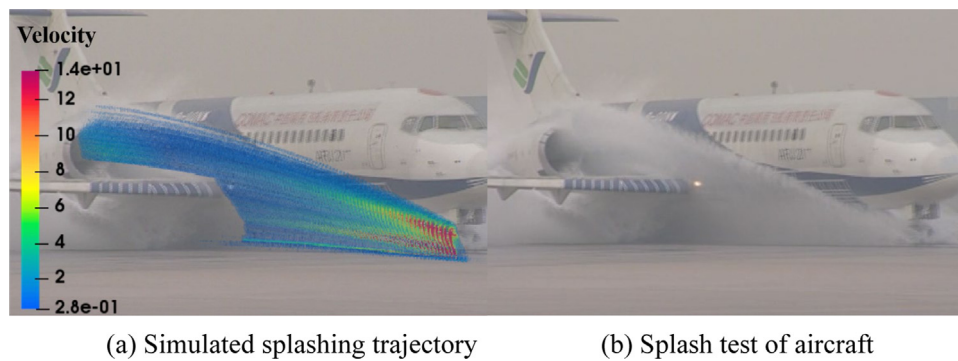


Fig. 15. Comparison between simulation result and experimental result.

of the engine flow field greatly influences the droplet's trajectory in the X direction, so the elevation angle of the spray changes. According to Fig. 10(b), the angle between the nose gear and the engine upper edge is 12.5 degrees. The angle between the nose gear and the engine center is 11.7 degree. The angle between the nose gear and the wing upper edge is 10.8 degrees.

(1) When the elevation angle of spray exceeds 11.7 degrees, the effect of the engine flow field on the splashing droplets is downward suction, which will reduce the elevation angle.

(2) When the elevation angle of spray exceeds 12.5 degrees, the upper edge of the splashing trajectory exceeds the upper edge of the engine, which is far away from the axial direction of the engine. Therefore, the splashing droplets are less affected by the engine suction, and the reduction of elevation angle is limited.

(3) When the elevation angle of spray is between 10.8 degrees and 11.7 degrees, the engine flow field has an upward suction on the splashing droplets, which will increase the elevation angle.

#### 4.2. Comparison with splash test

In addition to the engine flow field, the influence of crosswind should be considered in the test conditions. One of the test conditions is the aircraft speed of 90 knots, the crosswind of 5 m/s and the crosswind direction of 30 degrees. The splashing trajectory under this condition is calculated. The information of complete splashing trajectory is imported into Paraview, and a velocity cloud of the spray pattern is obtained by interpolation in Paraview, as shown in Fig. 15.

The simulated spray patterns are in good agreement with the experimental splashing trajectory, which proves the effectiveness

of the calculation method in this paper. Compared with calculating the complete splashing trajectory in LS-DYNA, the calculation time of the method in this paper is greatly reduced. In LS-DYNA, when the spray is formed, the smooth length changes due to the dispersion of SPH particles, and the calculation time increases rapidly. The calculation time of each time step reaches two hours, and it is difficult to consider the influence of air and engine flow field. This method proposed in this paper can not only greatly shorten the calculation time, which takes only 8 h to calculate the complete splashing trajectory on the personal computer, but also can consider the influence of air flow field, engine flow field and crosswind.

The splashing trajectory at the speed of 90 knots without the influence of crosswind is calculated. The influence of crosswind on the spray patterns is analyzed according to the calculation results, and the calculation results are shown in Fig. 16. It can be seen from Fig. 16 that the crosswind has a significant influence on the spray patterns. The crosswind perpendicular to the aircraft motion direction has an obvious influence on the front view angle, and the crosswind that is collinear with the aircraft motion direction will lead to the limited change of the elevation angle.

#### 4.3. Calculation of water inflow of engine

Whether a splashing particle enters the engine is mainly determined according to the position of the splashing particle. The boundary condition of the engine inlet is imported into the calcu-

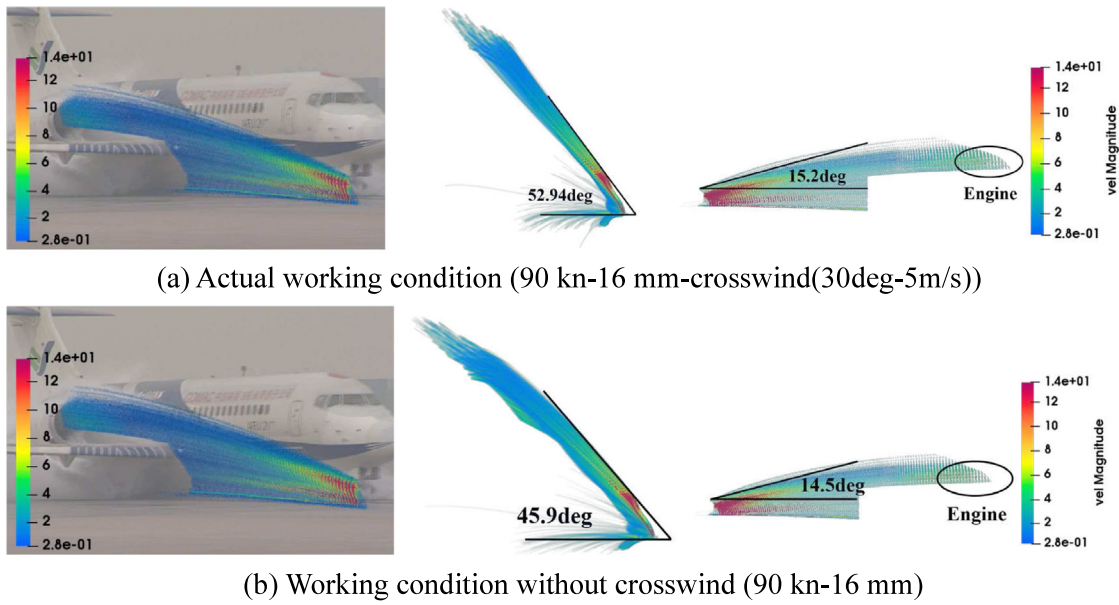
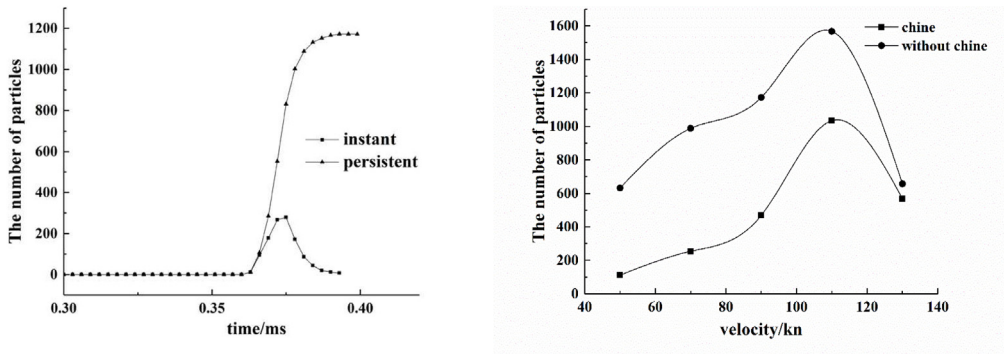


Fig. 16. Comparison of simulated splashing trajectory under different working conditions.



(a) The distribution under 90 knots of speed (b) Comparison under different speed conditions

Fig. 17. The statistics of water inflow of engine.

lation program. If the particle's position is within the range of the engine inlet, it is considered that the engine inhales the particle, and the particle ID is counted. Since the particles entering the engine inlet will be counted repeatedly in different time steps, the repeatedly calculated splashing particles are deleted to obtain the number curve of water inflow sucked by the engine at different times, as shown in Fig. 17(a) instant curve. Then, the water inflow at each time is accumulated to obtain the continuous water inflow, as shown in Fig. 17(a) persistent. It can be seen from Fig. 17(a) that after the tire spray is formed for some time, the water inflow of the engine remains stable. The water inflow of the engine under different working conditions is obtained in the same way, as shown in Fig. 17(b).

As shown from Fig. 17(b), when the sliding speed is lower than 90 knots, the chine has an obvious inhibition effect on the water inflow of the engine, but the inhibition effect decreases significantly when the sliding speed exceeds 110 knots. When the speed exceeds 110 kn, the tire has entered the hydroplaning state. When the water film completely lifts the tire, the chine height also increases, which will weaken the inhibition effect of tire spray.

### 5. Conclusions

- (1) The SPH–FEM coupling method is used to establish the water spray model of unilateral chine tire. The tire spray under different working conditions is simulated, and the influence law of different working conditions on the spray patterns is obtained. The elevation angle and front view angle first increase and then decrease with the increase of sliding speed, and the inflection point appears at the sliding speed. After the tire enters the hydroplaning state, the suppression effect of chine on water spray will be significantly weakened.
- (2) A more efficient and accurate calculation method for simulating the complete splashing trajectory in the complex flow field is proposed. In LS-DYNA, the SPH method is used to obtain the information of initial tire spray patterns, and the engine flow field is simulated in CFX. Then, the splashing particles are regarded as droplets, and the complete splashing trajectory of a tire under the influence of engine flow field and crosswind is obtained. The results are in good agreement with those of the splash test, which proves the effectiveness of this calculation method. The calculation method can consider the influence of a complex flow field, and the calculation time is greatly reduced.

(3) Finally, this method can also obtain the engine water inflow under different working conditions. The tire chine obviously suppresses the engine water inflow when the sliding speed is lower than hydroplaning speed. When the sliding speed exceeds hydroplaning speed, tire chine's effect of suppressing engine water inflow is not obvious.

### Declaration of competing interest

The authors declare the following financial interests/personal relationships which may be considered as potential competing interests: Decheng Wan reports financial support was provided by Shanghai Jiao Tong University.

### Data availability

The data that support the findings of this study are available from the corresponding author upon reasonable request.

### Acknowledgments

This work is supported by the National Key Research and Development Program of China (2019YFB1704200), and the National Natural Science Foundation of China (52131102, 51879159), to which the authors are most grateful.

### References

- [1] G.W.H. Van Es, A.L.C. Roelen, E.A.C. Kruijssen, et al., Safety aspects of aircraft performance on wet and contaminated runways, in: 10th Annual European Aviation Safety Seminar, National Aerospace Laboratory, Amsterdam, 1998.
- [2] Certification Specifications and Acceptable Means of Compliance for Large Aeroplanes, CS-25 Amendment, EASA, 2011.
- [3] Water Ingestion Testing for Turbine Powered Airplanes, FAA AC 20-124, FAA, 1985.
- [4] Takeoff Performance Data for Operations on Contaminated Runways, AC 25-31, FAA, 2015.
- [5] L. Lel, G. Taylor, An Investigation of the Influence of Aircraft Tire-Tread Wear on Wet-Runway Braking, NASA TN D-2770, 1965.
- [6] R.C. Dreher, W.B. Horne, Ground-Run Tests with a Bogie Landing Gear in Water and Slush, NASA TN D-3515, NASA, Washington, D.C., 1966.
- [7] C.S. Martin, Hydrodynamics of tire hydroplaning, *J. Aircr.* 4 (2) (1967) 136–140.
- [8] R.V. Barrett, Drag and Spray Measurements from a Pair of Small Pneumatic Tyres and Placed Side By Side, Ministry of Aviation, Technical Information and Library Services, 1965.
- [9] R.V. Barrett, Measurements of the Drag and Spray Produced By Model Pneumatic Wheels Moving Through Water Layers, (Ph.D. thesis), University of Bristol, London, 1967.
- [10] R.V. Barrett, Wheel Spray and Aqua-Planning At Bristol University using Small Pneumatic Tyres, Research Into Slush Drag, Ministry of Defence, 1970.
- [11] Estimation of Spray Patterns Generated from the Sides of Aircraft Tyres Running in Water Or Slush, ESDU 83042, ESDU, 1998.
- [12] L.G. Trapp, G.L. Oliveira, Aircraft thrust reverser cascade configuration evaluation through CFD, in: 41st Aerospace Sciences Meeting and Exhibit, in: AIAA-2003-0723, American Institute of Aeronautics & Astronautics, Reno, Nevada, 2003.
- [13] J.H.M. Gooden, The effect of crosswind on engine ingestion during take-offs from water contaminated runways, in: 28th International Congress of the Aeronautical Sciences, 2012.
- [14] J.H.M. Gooden, Engine Ingestion As a Result of Crosswind During Take-Offs from Water Contaminated Runways, NLR-TP-2013-201, 2013.
- [15] Q.L. Qu, F. Zhang, P.Q. Liu, et al., Numerical simulation of water spray caused by a rolling airplane tire, *J. Aircr.* 53 (1) (2016) 182–188.
- [16] K. Zhao, P.Q. Liu, Q.L. Qu, et al., Numerical simulation of aircraft tire-generated spray and engine ingestion on flooded runways, *J. Aircr.* (2017) 1–9.
- [17] K. Zhao, P.Q. Liu, Q.L. Qu, et al., Flow physics and chine control of the water spray generated by an aircraft rigid tire rolling on contaminated runways, *Aerosp. Sci. Technol.* 72 (2018) 49–62.
- [18] X.P. Zhang, F. Xu, X.Q. Ren, et al., Consideration on aircraft tire spray when running on wet runways, *Chin. J. Aeronaut.* (2019).
- [19] X.P. Zhang, F. Xu, X.Q. Ren, et al., Similarity of spray generated by tire rolling in the water and falling in water, *Sci. Sinica Technol.* 48 (09) (2018) 931–938, (in Chinese).
- [20] X.S. Guan, F. Xu, M.Q. Hu, X.Q. Ren, Numerical simulation of water spray generated by aircraft multi-wheels, *Int. J. Comput. Fluid Dyn.* 35 (1–2) (2021).
- [21] G. Chaussonnet, S. Braun, T. Dauch, et al., Toward the development of a virtual spray test-rig using the smoothed particle hydrodynamics method, *Comput. & Fluids* 180 (2019) 68–81.
- [22] J.R. Cho, H.W. Lee, J.S. Sohn, et al., Numerical investigation of hydroplaning characteristics of three-dimensional patterned tire, *Eur. J. Mech. A* (2006).
- [23] A. Baines, P. Watson, L.S. Cunningham, et al., Modelling shore-side pressure distributions from violent wave breaking at a seawall, *Eng. Comput. Mech.* 172 (3) (2019) 1–14.
- [24] X. Wen, W. Zhao, D. Wan, Multi-phase moving particle semi-implicit method for violent sloshing flows, *Eur. J. Mech. B* 95 (2022) 1–22.
- [25] G. Zhang, W. Zhao, D. Wan, Numerical simulations of sloshing waves in vertically excited square tank by improved MPS method, *J. Hydrodyn.* 34 (1) (2022) 76–84.
- [26] X. Wen, W. Zhao, D. Wan, Numerical simulations of multi-layer-liquid sloshing by multiphase MPS method, *J. Hydrodyn.* 33 (5) (2021) 938–949.
- [27] X. Wen, W. Zhao, D. Wan, A multiphase MPS method for bubbly flows with complex interfaces, *Ocean Eng.* 238 (2021) 109743.
- [28] M.B. Liu, Z. Zong, J.Z. Chang, Developments and applications of smoothed particle hydrodynamics, *Adv. Mech.* 41 (2011) 217–234, (in Chinese).
- [29] M.B. Liu, G.R. Liu, K.Y. Lam, et al., Smoothed particle hydrodynamics for numerical simulation of underwater explosion, *Comput. Mech.* 30 (2) (2003) 106–118.
- [30] H. Gotoh, A. Khayyer, Y. Shimizu, Entirely Lagrangian meshfree computational methods for hydroelastic fluid–structure interactions in ocean engineering—Reliability, adaptivity and generality, *Appl. Ocean Res.* 115 (2021) 102822.
- [31] H.G. Lyu, P.N. Sun, X.T. Huang, et al., A review of SPH techniques for hydrodynamic simulations of ocean energy devices, *Energies* 15 (2) (2022) 502.
- [32] Z. Li, J. Leduc, J. Nunez-Ramirez, et al., A non-intrusive partitioned approach to couple smoothed particle hydrodynamics and finite element methods for transient fluid–structure interaction problems with large interface motion, *Comput. Mech.* 55 (2015) 697–718.
- [33] C. Hermange, G. Oger, Y.L. Chenadec, et al., A 3D SPH–FE coupling for FSI problems and its application to tire hydroplaning simulations on rough ground, *Comput. Methods Appl. Mech. Engrg.* 355 (2019) 558–590.
- [34] J. Pelfrene, S. Kameswara, S. Vepa, et al., Study of the SPH Method for Simulation of Regular and Breaking Waves, gent universiteit gent, 2011.
- [35] S. Lee, J.W. Hong, Parametric studies on smoothed particle hydrodynamic simulations for accurate estimation of open surface flow force, *Int. J. Nav. Archit. Ocean Eng.* 12 (2020) 85–101.
- [36] Lee Ko, Hong, Comparative study on the breaking waves by a piston-type wavemaker in experiments and SPH simulations, *Coast. Eng. J.* (2020).
- [37] J.O. Hallquist, LS-DYNA Keyword User's Manual, Livermore Software Technology Corporation, 2007.
- [38] J.J. Monaghan, R.A. Gingold, Shock simulation by the particle method SPH, *J. Comput. Phys.* 52 (2) (1983) 374–389.
- [39] X.J. Li, C.J. Zhang, X.H. Wang, et al., Numerical study on the effect of equations of state of water on underwater explosions, *Eng. Mech.* 31 (08) (2014) 46–52, (in Chinese).
- [40] H. Yang, M. Fan, A. Liu, et al., General formulas for drag coefficient and settling velocity of sphere based on theoretical law, *Int. J. Mining Sci. Technol.* (2015).